

Classification of Tidal Disruption Events Based on Stellar Orbital Properties

Kimitake HAYASAKI¹, Shiyang ZHONG², Shuo LI³, Peter BERCZIK^{3,4,5}, and Rainer SPURZEM^{3,4,6}

kimi@cbnu.ac.kr

Received _____; accepted _____

¹Department of Astronomy and Space Science, Chungbuk National University, Cheongju 361-763, Korea

²Yunnan Observatories, Chinese Academy of Sciences, 396 Yang-Fang-Wang, Guandu District, 650216, Kunming, Yunnan, China

³National Astronomical Observatories of China and Key Laboratory for Computational Astrophysics, Chinese Academy of Sciences, 20A Datun Rd., Chaoyang District, 100012, Beijing, China

⁴Astronomisches Rechen-Institut, Zentrum für Astronomie, University of Heidelberg, Mönchhofstrasse 12-14, D-69120 Heidelberg, Germany

⁵Main Astronomical Observatory, National Academy of Sciences of Ukraine, 27 Akademika Zabolotnoho St., 03680 Kyiv, Ukraine

⁶Kavli Institute for Astronomy and Astrophysics, Peking University, 100871 Beijing, China

ABSTRACT

We study the rates of tidal disruption of stars by intermediate-mass to supermassive black holes on bound to unbound orbits by using high-accuracy direct N-body experiments. The approaching stars from the star cluster to the black hole can take three types of orbit: eccentric, parabolic, and hyperbolic orbits. Since the mass fallback rate shows a different variability depending on these orbital types, we can classify tidal disruption events (TDEs) into three main categories: eccentric, parabolic, and hyperbolic TDEs. Respective TDEs are characterized by two critical values of the orbital eccentricity: the lower critical eccentricity is the one below which the stars on eccentric orbits cause the finite, intense accretion, and the higher critical eccentricity above which the stars on hyperbolic orbits cause no accretion. Moreover, we find that the parabolic TDEs are divided into three subclasses: precisely parabolic, marginally eccentric, and marginally hyperbolic TDEs. We analytically derive that the mass fallback rate of the marginally eccentric TDEs can be flatter and slightly higher than the standard fallback rate proportional to $t^{-5/3}$, whereas it can be flatter and lower for the marginally hyperbolic TDEs. We confirm by N-body experiments that only few eccentric, precisely parabolic, and hyperbolic TDEs can occur in a spherical stellar system with a single intermediate-mass to supermassive black hole. A substantial fraction of the stars approaching to the black hole would cause the marginally eccentric or marginally hyperbolic TDEs.

Subject headings: accretion, accretion disks – black hole physics – galaxies: nuclei
- galaxies: star clusters: general – stars: kinematics and dynamics – methods:
numerical

1. Introduction

Tidal disruption events (TDEs) are thought to be a key phenomenon for searching dormant supermassive black holes (SMBHs) at the centers of the inactive galaxies or intermediate-mass black holes (IMBHs) at those of the star clusters. Most TDEs take place when a star at large separation (~ 1 pc) is perturbed onto a parabolic orbit approaching close enough to the SMBH to be ripped apart by its tidal force. The subsequent accretion of stellar debris falling back to the SMBH causes a characteristic flare with a luminosity large enough to exceed the Eddington luminosity for a time scale of weeks to months (Rees 1988; Phinney 1989; Evans & Kochanek 1989). Such flares have been discovered at optical (Gezari et al. 2012; Arcavi et al. 2014; Holoiën et al. 2014; Hung et al. 2017), ultraviolet (Gezari et al. 2006; Chornock et al. 2014; Vinkó et al. 2015), and soft X-ray (Komossa & Bade 1999; Saxton et al. 2012; Maksym et al. 2013; Auchettl et al. 2017) wavelengths with inferred event rates of $10^{-4} - 10^{-5}$ per year per galaxy (Donley et al. 2002; Wang & Merritt 2004; van Velzen & Farrar 2014; Stone & Metzger 2016). The other, high-energy jetted TDEs have been detected through non-thermal emissions in radio (Zauderer et al. 2011; Alexander et al. 2016; van Velzen et al. 2016) or hard X-ray (Burrows et al. 2011; Brown et al. 2015) wavelengths with much lower event rate (Farrar & Piran 2014).

TDEs can largely contribute to the growth of the relatively low-mass SMBHs ($\lesssim 10^6 M_\odot$) or IMBHs because of the lack of large amount of gas in their environments, although the rate of the tidal disruption is relatively low. The growth rate depends on the stellar density profile (Bahcall 1976) and timescale of mass supply in the star cluster based on the classical loss cone theory (Frank & Rees 1976). Baumgardt et al. (2004) examined the cluster density profile and the effect of the TDEs on the black hole growth by performing the self-consistent N-body simulations of star clusters composed of equal-mass stars and a central, IMBH. Subsequently, Brockamp et al. (2011) calculated the tidal disruption rate

of stars by SMBHs by performing higher resolution N-body simulations. They concluded that relaxation-driven stellar feeding cannot let the black hole grow to more than $10^7 M_{\odot}$. Although the standard two-body scattering mechanism for generating TDEs (Magorrian & Tremaine 1999; Wang & Merritt 2004) predicts effectively parabolic trajectories, recent high-accuracy direct N-body simulations show that a significant amount of stars entering the tidal disruption radius has the orbital eccentricities less or more than 1.0 (Zhong et al. 2014).

It still remains under debate how the standard, theoretical mass fallback rate proportional to $t^{-5/3}$ (Rees 1988; Phinney 1989; Evans & Kochanek 1989) translates into the observed light curves. While most of the soft X-ray TDEs appear to follow the $t^{-5/3}$ power law decay curve proportional to the fallback rate (see Komossa 2015 for a review), the optical to ultraviolet TDEs exhibit the different decay curve (Gezari et al. 2012; Chornock et al. 2014; Arcavi et al. 2014; Holoien et al. 2014).

Lodato et al. (2009) numerically showed that the fallback rate depends on the internal structure of the tidally disrupted stars, leading to early-time deviations from the standard fallback rate. The centrally condensed core survived by the partial disruption of the star can let the resultant light curves steeper (Guillochon & Ramirez-Ruiz 2013). The accretion of clumps formed by the self-gravity of the debris stream causes the significant variations of the light curve around the $t^{-5/3}$ average at late times (Coughlin & Nixon 2015). The outflows or winds caused during the super-Eddington accretion phase lets the optical to ultraviolet light curves deviated from the standard $t^{-5/3}$ curve (Strubbe & Quataert 2009; Lodato & Rossi 2011). There have been some arguments that the energy dissipated by the stream-stream collisions during the debris circularization powers the observed optical to ultraviolet TDEs (Piran et al. 2015; Jiang et al. 2016; Bonnerot et al. 2017).

Recent hydrodynamic simulations have shown that observable properties of these

“eccentric” TDEs significantly deviate from those of standard TDEs; in particular, the rate of mass return is substantially increased by being cut off at a finite time, rather than continuing indefinitely as a power law decay (Hayasaki et al. 2013, 2016). This suggests that the variability of TDE light curves also depends on the orbital type of approaching stars, especially orbital eccentricity and penetration factor (which is the ratio of the tidal disruption radius to pericenter distance of the star) of stars.

In this paper, we classify the TDEs by the type of orbits of stars approaching to SMBHs or IMBHs, and examine each occurrence rate in the dense star cluster system modeled by N-body experiments. In Section 2, we give a condition to classify the TDEs by the type of the stellar orbits, and analytically derive the mass fallback rate of each TDE based on the condition, which can have the different time dependence from the standard fallback rate proportional to $t^{-5/3}$. In Section 3, we describe our numerical approach and simulations results, where we mainly focus on the eccentricity distribution of the N-body particles for their penetration factor. We discuss the reality of our simulation results by using the scaling method to extrapolate them in Section 4. Finally, Section 5 is devoted to conclusion of our scenario.

2. Type of tidal disruption events

As a star approaches and enters into the tidal disruption radius of the SMBH or IMBH, it is disrupted by the tidal force of the black hole which dominating the stellar self-gravity and pressure forces at the tidal disruption radius:

$$r_t = \left(\frac{M_{\text{bh}}}{m_*}\right)^{1/3} r_* \approx 24 \left(\frac{M_{\text{bh}}}{10^6 M_\odot}\right)^{-2/3} \left(\frac{m_*}{M_\odot}\right)^{-1/3} \left(\frac{r_*}{R_\odot}\right) r_S. \quad (1)$$

Here we denote the black hole mass with M_{bh} , stellar mass with m_* and radius with r_* , and the Schwarzschild radius with $r_S = 2GM_{\text{bh}}/c^2$, where G and c are Newton’s gravitational

constant and the speed of light, respectively. The tidal force then produces a spread in specific energy of the stellar debris:

$$\Delta\epsilon \approx \frac{GM_{\text{bh}}r_*}{r_t^2} \quad (2)$$

(Evans & Kochanek 1989).

2.1. Critical value of orbital eccentricity and semi-major axis

The specific energy of the tidally disrupted star ranges over

$$-\Delta\epsilon + \epsilon_{\text{orb}} \leq \epsilon \leq \Delta\epsilon + \epsilon_{\text{orb}}. \quad (3)$$

Here ϵ_{orb} is the specific orbital energy of the star approaching to the black hole:

$$\epsilon_{\text{orb}} = \begin{cases} -\frac{GM_{\text{bh}}}{2r_t}\beta(1-e) & \text{eccentric or circular orbit : } (0 \leq e < 1) \\ 0 & \text{parabolic orbit : } (e = 1) \\ \frac{GM_{\text{bh}}}{2r_t}\beta(e-1) & \text{hyperbolic orbit : } (e > 1), \end{cases} \quad (4)$$

where e and β are the orbital eccentricity of the approaching star and the penetration factor, respectively. The penetration factor is defined by r_t/r_p , where r_p is the pericenter distance: $r_p = a(1-e)$ for eccentric orbits and $r_p = a(e-1)$ for hyperbolic orbits. In the standard TDE scenario that a star is disrupted from a parabolic orbit, the debris mass will be centered on zero and distributed over $-\Delta\epsilon \leq \epsilon \leq \Delta\epsilon$ because of $\epsilon_{\text{orb}} = 0$ (Rees 1988; Evans & Kochanek 1989).

Since the stellar debris with negative specific energy is bound to the black hole, it returns to pericenter and will eventually accrete onto the black hole. For eccentric orbits, if $\Delta\epsilon + \epsilon_{\text{orb}} \leq 0$ in equation (3), all the stellar debris should be bounded by the black hole even after the tidal disruption, and eventually fallbacks to the black hole. The condition

$\epsilon_{\text{orb}} = -\Delta\epsilon$ therefore gives a critical value of orbital eccentricity of the star

$$e_{\text{crit},1} = 1 - 2\frac{q^{-1/3}}{\beta}, \quad (5)$$

below which all the stellar debris should remain gravitationally bound to the black hole, where the ratio of the black hole to stellar mass is defined by $q \equiv M_{\text{bh}}/m_*$.

In contrast, if $-\Delta\epsilon + \epsilon_{\text{orb}} \leq 0$ in equation (3) for the hyperbolic orbits, a part of the stellar debris should be bounded by the black hole and eventually fallbacks to the black hole. The condition $\epsilon_{\text{orb}} = \Delta\epsilon$ also gives a critical value of orbital eccentricity of the star

$$e_{\text{crit},2} = 1 + 2\frac{q^{-1/3}}{\beta} \quad (6)$$

below which a part of the stellar debris should remain gravitationally bound to the black hole.

These critical eccentricities give us the condition that the tidal disruption flare can happen in terms of the orbital eccentricity of the star:

$$\left\{ \begin{array}{ll} 0 \leq e < e_{\text{crit},1} & \text{eccentric TDEs} \\ e_{\text{crit},1} \leq e \leq e_{\text{crit},2} & \text{parabolic TDEs} \\ e_{\text{crit},2} < e & \text{hyperbolic TDEs.} \end{array} \right. \quad (7)$$

Alternatively, we can define the critical value to classify the TDEs from the viewpoints of the semi-major axis as follows:

$$\left\{ \begin{array}{ll} 0 < a < a_c & \text{eccentric TDEs} \\ a_c \leq a & \text{parabolic TDEs} \\ 0 < a < a_c & \text{hyperbolic TDEs,} \end{array} \right. \quad (8)$$

where $\epsilon_{\text{orb}} < 0$ for the eccentric TDEs and $\epsilon_{\text{orb}} > 0$ for the hyperbolic TDEs, and a_c is defined by

$$a_c \equiv \frac{q^{1/3}}{2} r_t = 50 \left(\frac{q}{10^6} \right)^{1/3} r_t. \quad (9)$$

Panel (a) of Figure 1 shows the dependence of critical eccentricities on the penetration factor β with the fixed value of $M_{\text{bh}} = 10^6 M_{\odot}$, whereas Panel (b) shows the dependence of critical eccentricities on the mass ratio q with the fixed value of $\beta = 1$. In both panels, red and blue shaded regions show the eccentric and hyperbolic TDEs, respectively. The white shaded region between the blue and red solid lines show the parabolic TDEs. From the both panels, the higher value of β and the more massive black holes tend to produce the different type of TDEs by the slighter difference of the critical eccentricity.

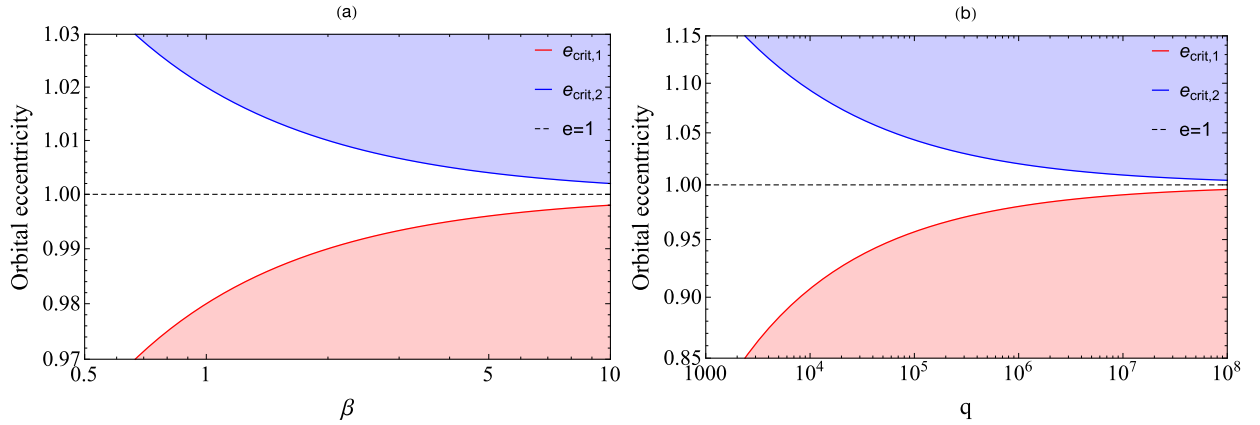


Fig. 1.— Dependence of critical eccentricities on the penetration factor β and the ratio of the black hole to stellar mass $q = M_{\text{bh}}/m_*$. Panel (a) shows the dependence of the critical eccentricity on β with the fixed value of $M_{\text{bh}} = 10^6 M_{\odot}$. Panel (b) shows the dependence of critical eccentricity on q with the fixed value of $\beta = 1$. In both panels, red and blue shaded area show the regions of eccentric and hyperbolic TDEs, respectively. The white shaded area between the blue and red solid lines show the region of parabolic TDEs.

2.2. Modification of mass fallback rates

Following Evans & Kochanek (1989), the mass fallback rate is given by

$$\frac{dM}{dt} = \frac{dM}{d\epsilon} \frac{d\epsilon}{dt}, \quad (10)$$

where $dM/d\epsilon$ is the differential mass distribution of the stellar debris with specific energy ϵ . Because the thermal energy of the stellar debris is negligible compared with the binding energy, $\epsilon \approx \epsilon_d$, where ϵ_d is defined as the specific binding energy of the stellar debris by

$$\epsilon_d \equiv -\frac{GM_{\text{bh}}}{2a_d}, \quad (11)$$

and by applying the Kepler's third law to it we obtain that

$$\frac{d\epsilon_d}{dt} = \frac{1}{3}(2\pi GM_{\text{bh}})^{2/3} t^{-5/3}. \quad (12)$$

Here, we newly assume that

$$\frac{dM}{d\epsilon} \equiv \frac{\eta_1(\alpha, a)}{2} \frac{m_*}{\Delta\epsilon} \left(\frac{-\epsilon_d}{\Delta\epsilon} \right)^\alpha \quad (\epsilon_d < 0), \quad (13)$$

where α is the power law index and $\eta_1(\alpha, a)$ is the normalization coefficient obtained by the finite integral: $\int_{-\Delta\epsilon+\epsilon_{\text{orb}}}^{\epsilon_{\text{orb}}} (dM/d\epsilon) d\epsilon'_d = m_*/2$ as

$$\eta_1(\alpha, a) \equiv (\alpha + 1) \left[\left(1 + \frac{a_c}{a} \right)^{\alpha+1} - \left(\frac{a_c}{a} \right)^{\alpha+1} \right]^{-1}. \quad (14)$$

It is required that $\alpha + 1$ is greater than zero because of $0 \leq \eta_1(\alpha, a) < \infty$. If $\alpha = 0$ is adopted, equation (13) is reduced, independently of the semi-major axis of the approaching star, to the top-hat distribution around zero specific energy: $dM/d\epsilon = m_*/(2\Delta\epsilon)$ proposed by Rees (1988). The non-zero value of α represents the effect of the density profile of the star on $dM/d\epsilon$. In the limit of $a \rightarrow \infty$, equation (13) is applicable to estimating $dM/d\epsilon$ of the centrally condensed stars on parabolic orbits (Lodato et al. 2009) or the partially disrupted stars on parabolic orbits (Guillochon & Ramirez-Ruiz 2013). In the case of

eccentric TDEs, $dM/d\epsilon$ has a different distribution from the top-hat one (Hayasaki et al. 2013). This implies that $dM/d\epsilon$ of non-parabolic TDEs can deviate from the standard, top-hat distribution. Since $dM/d\epsilon$ is a decreasing function of $-\epsilon_d$, α should be less than or equal to zero. The possible range of α is therefore given by $-1 < \alpha \leq 0$.

The specific binding energy of the most tightly bound debris is given by

$$\epsilon_{\text{mtb}} = -\Delta\epsilon \pm \frac{GM_{\text{bh}}}{2a},$$

where negative and positive signs of the second term of the right-hand side originate from the originally approaching stars on eccentric and hyperbolic orbits, respectively. It is easily confirmed that ϵ_{mtb} is reduced to be that of precisely parabolic orbit ($e = 1$) in the limit of $a \rightarrow \infty$. The orbital period of the most tightly bound debris is proportional to $\epsilon_{\text{mtb}}^{-3/2}$ from the Kepler's third law:

$$t_{\text{mtb}} = \sqrt{\frac{4\pi^2}{GM_{\text{bh}}}} a_c^{3/2} \left(1 \mp \frac{a_c}{a}\right)^{-3/2} \quad (a \geq a_c). \quad (15)$$

Substituting equations (12) and (13) into equation (10) with equations (11) and (15), we obtain the modified fallback rate:

$$\frac{dM}{dt} = \frac{\eta_2(\alpha, a)}{3} \left(\frac{m_*}{t_{\text{mtb}}}\right) \left(\frac{t}{t_{\text{mtb}}}\right)^{-2\alpha/3-5/3}, \quad (16)$$

where $\eta_2(\alpha, a)$ is the proportional coefficient defined by

$$\eta_2(\alpha, a) \equiv (\alpha + 1) \left(1 \mp \frac{a_c}{a}\right)^{\alpha+1} \left[\left(1 + \frac{a_c}{a}\right)^{\alpha+1} - \left(\frac{a_c}{a}\right)^{\alpha+1} \right]^{-1} \quad (17)$$

with the upper and lower signs corresponding to the hyperbolic and eccentric orbit cases, respectively. Note that $\eta_2(\alpha, a)$ should be greater than or equal to zero in order for $dM/dt \geq 0$. The relation between η_2 and η_1 is given by $\eta_2(\alpha, a) = \eta_1(\alpha, a)(1 \mp a_c/a)^{\alpha+1}$ from equations (14) and (17). The possible range of α for a given value of a is therefore $-1 < \alpha \leq 0$ in equation (16). For both the eccentric and hyperbolic orbit cases, the possible

range of a is $a_c \leq a < \infty$. In the limit of the parabolic orbit ($a \rightarrow \infty$), $\eta_2(\alpha, a)$ is reduced to $\alpha + 1$. For the hyperbolic orbit case, $\eta_2(\alpha, a)$ is always smaller than unity, and $\eta_2(\alpha, a_c) = 0$ at the equality of $a = a_c$. This equality means that the star approaches the black hole on such a hyperbolic orbit that no debris fallbacks after the tidal disruption. These arguments imply that the parabolic TDEs are divided into three subclasses: marginally eccentric ($e_{\text{crit},1} \leq e < 1$), standard, precisely parabolic ($e = 1$), and marginally hyperbolic ($1 < e \leq e_{\text{crit},2}$) TDEs. For useful purpose, we summarize the classification of TDEs in Table 1.

For marginally eccentric TDEs, the mass fallback rate takes a maximum at $a = a_c$ and $\alpha = 0$. While the mass fallback rate is proportional to $t^{-5/3}$ for $\alpha = 0$, it more loosely decays with time for $-1 < \alpha < 0$. For precisely parabolic TDEs ($a \rightarrow \infty$), equation (16) reduces to $dM/dt = (\alpha + 1)/3(m_*/t_{\text{mtb}})(t/t_{\text{mtb}})^{-2\alpha/3-5/3}$. If $\alpha = 0$ is adopted, it corresponds to equation (3) of Evans & Kochanek (1989): $dM/dt = (1/3)(m_*/t_{\text{mtb}})(t/t_{\text{mtb}})^{-5/3}$. For marginally hyperbolic TDEs, the mass fallback rate takes a maximum at $a \rightarrow \infty$ and $\alpha = 0$, and is close to zero as $a \rightarrow a_c$. It more loosely decays with time for $-1 < \alpha < 0$ as is the case with the marginally eccentric TDEs. For the hyperbolic TDEs ($e_{\text{crit},2} < e$), the mass fallback rate should be zero. In other words, all the debris mass are unbound to the black hole. The hyperbolic TDEs cannot thus contribute to the event rate of the tidal disruption, even if they might occur. The current formula of dM/dt significantly underestimates the mass fallback rate of eccentric TDEs ($0 \leq e < e_{\text{crit},1}$), because $dM/d\epsilon$ would not follow a simple power law but have more like a Gaussian distribution if the specific binding energy of most loosely bound orbit is negative enough beyond $-\Delta\epsilon$ (Hayasaki et al. 2013). Our conjecture given by equation (13) should be therefore inapplicable to eccentric TDEs.

Table 1. Summary for classification of TDEs. The first column represents the type of the TDEs. The second column shows the condition to classify the TDEs from the viewpoints of the orbital eccentricity, e , with two critical eccentricities $e_{\text{crit},1}$ and $e_{\text{crit},2}$ (see equations (5)-(7)). The third column shows the condition from the viewpoint of the semi-major axis, a , with the critical semi-major axis a_c (see equations (8) and (9)). The fourth column denotes the possible range of α for each TDE. The final column represents the mass fallback rate for each TDE, where $\eta_2(\alpha, a)$ is the proportional coefficient given by equation (17) and t_{mtb} is the orbital period of the most tightly bound orbit given by equation (15).

Type of TDEs	e	a	α	dM/dt
Eccentric	$0 \leq e < e_{\text{crit},1}$	$0 < a < a_c$	—	Intense accretion*
Marginally eccentric	$e_{\text{crit},1} \leq e < 1$	$a_c \leq a < \infty$	$-1 < \alpha \leq 0$	$(\eta_2(\alpha, a)/3)(m_*/t_{\text{mtb}})(t/t_{\text{mtb}})^{-2\alpha/3-5/3}$
Precisely parabolic	$e = 1$	$a \rightarrow \infty$	$-1 < \alpha \leq 0$	$(1/3)(\alpha + 1)(m_*/t_{\text{mtb}})(t/t_{\text{mtb}})^{-2\alpha/3-5/3**}$
Marginally hyperbolic	$1 < e \leq e_{\text{crit},2}$	$a_c \leq a < \infty$	$-1 < \alpha \leq 0$	$(\eta_2(\alpha, a)/3)(m_*/t_{\text{mtb}})(t/t_{\text{mtb}})^{-2\alpha/3-5/3}$
Hyperbolic	$e_{\text{crit},2} < e$	$0 < a < a_c$	—	No accretion

*see Hayasaki et al. (2013)

**It corresponds to equation (3) of Evans & Kochanek (1989) if $\alpha = 0$ is adopted.

3. N-body experiments

In this section, we present a scaling study of whether there are five (three plus two) types of TDEs from the viewpoint of the stellar orbits by N-body experiments, and estimate the fractional number of each event rate. All the simulations are performed by using the massively parallel ϕ -GRAPE code (Harfst et al. 2007), with high performance up to 1.5 Tflop/s per GPU on our HPC clusters in Beijing (NAOC/CAS) and Heidelberg (ARI/ZAH) (Berczik et al. 2011; Spurzem et al. 2012; Berczik et al. 2013a,b). The code is a direct N-body simulation package, with a high order Hermite integration scheme and individual block time steps. A direct N-body code evaluates in principle all pairwise forces between the gravitating particles, and its computational complexity scales asymptotically with N^2 ; however, it is not to be confused with a simple brute force shared time step code, due to the block time steps. The present code is well-tested and already used to obtain important results in our earlier large scale (up to few million body) simulation (Khan et al. 2012; Zhong et al. 2014; Khan et al. 2016; Li et al. 2017).

3.1. Method

We use the same simulation method as Zhong et al. (2014) here. In our simulations, $G = 1$, $M_c = 1$, $r_c = 1$, $E_c = -1/4$ (*Hénon units*) are adopted for useful purpose (Hénon 1971; Heggie & Mathieu 1986), where G , M_c , r_c , and E_c are the gravitational constant, the total mass of the cluster, the virial radius and energy of the star cluster, respectively.

We choose different values of N and introduce the normalized accretion radius $\xi_{\text{acc}} \equiv r_{\text{acc}}/r_c$ to evaluate the physical scaling behavior of our system and extrapolate to the real system. Here $N = M_c/m$ is the particle number, which defines the ratio between particle mass m and total mass of the system M_c . Note that m does not have to be identical

Table 2: Simulation parameters and results. The first column shows each model. The second, third, fourth, and fifth columns are the total number of N-body particles N in units of $K = 1024$, the accretion radius ξ_{acc} , and the number of accreted particles N_{acc} , and the simulation run time t_{end} , respectively. The sixth and seventh columns describe the normalized initial and final mass of the black hole, respectively. The last five columns represent the fractional number of the accreted particles on respective orbits in percent figures (%), where f_e , f_{me} , f_p , f_{mh} , and f_h are the fractional number of the eccentric, marginally eccentric, precisely parabolic, marginally hyperbolic, and hyperbolic TDEs, respectively (see Table 1 about the definition of each TDE). Each mass, size, and time are normalized by *Hénon units* ($G = 1$, $M_c = 1$, $r_c = 1$, and $E_c = -1/4$).

Model	N/K	ξ_{acc}	N_{acc}	t_{end}	μ_{ini}	μ_{end}	f_e	f_{me}	f_p	f_{mh}	f_h
1	128	10^{-5}	449	1500	0.01	0.01	0	95.6	0.2	4.2	0
2	128	10^{-4}	1972	700	0.01	0.01	0	28.9	0	71.1	0
3	256	10^{-5}	712	1500	0.01	0.01	0	75	0	25	0
4	256	10^{-4}	1035	400	0.01	0.01	0	19.1	0	80.9	0
5	512	10^{-5}	693	1000	0.01	0.01	0	54.3	0	45.7	0
6	128	10^{-5}	1141	900	0.05	0.05	0	91.1	0	8.9	0
7	128	10^{-4}	2433	500	0.05	0.05	0	29.82	0.08	70.1	0
8	256	10^{-5}	1318	700	0.05	0.05	0	67.5	0	32.5	0
9	256	10^{-4}	3763	500	0.05	0.05	0	22.3	0.0	77.7	0
10	512	10^{-5}	1854	600	0.05	0.05	0	45.95	0.05	54	0
11	128	10^{-5}	1171	2200	0.01	0.019	0	54	0	46	0
12	128	10^{-4}	8288	2450	0.01	0.073	0.2	87.8	0	12	0
13	128	10^{-3}	16620	2200	0.01	0.14	0.6	22.8	0	76.4	0.2
14	256	10^{-5}	1627	2522	0.01	0.018	0	39.3	0	60.7	0
15	256	10^{-4}	6651	1400	0.01	0.035	0	13.5	0	86.5	0

with the stellar mass. Currently adopted N is from 128K to 512K (see Table 2), where we define $1K = 1024$ due to technical reason through this paper, and a Plummer model is adopted for the initial stellar distribution (Aarseth et al. 1974).

The normalized accretion radius ξ_{acc} is another dimensionless number which defines a radius at which simulation particles are to be disrupted by tidal forces of a central black hole, relative to the virial radius of our system, which is used as standard unit. Extrapolation to the real system means that N is approaching real particle (star) numbers (like say 10^8 in galactic nuclei) and $\zeta \equiv r_{\text{acc}}/r_t$ is close to 1 at the same time. We also have a third dimensionless parameter in our models, which is $\mu = M_{\text{bh}}/M_c$. From the standard relations between galactic bulges and central massive black holes (Magorrian et al. 1998; McConnell & Ma 2013), it should be up to ~ 0.006 . However, we choose higher values because we only simulate part of the central star cluster mass; $\mu = (0.01, 0.05)$.

In our simulations, there are two type of sink particles; one is that the black hole is fixed with no accretion. In this case, the stars entering inside a finite accretion radius, corresponding to the tidal disruption radius, contribute no growth of the black hole and add no linear momentum to the black hole, and are right away removed from the stellar system. It looks unphysical but is enough to test which orbit the stars are tidally disrupted on. Another type is that the black hole particle simply gains the masses of the removed stars without adding their linear momentum. Once the star comes into the tidal disruption radius, it will be removed from the stellar system. The similar approaches we already implement in ϕ -GRAPE/GPU code and well tested against all the energy and momentum conservations in our earlier works (Just et al. 2012; Kennedy et al. 2016). The initial density profile of the Plummer model has a central flat core, which adjusts to the gravity of the central black hole during a few dynamical orbits, as is the case of Zhong et al. (2014). In any case, all the stars have equal mass and forms no binary stars through the simulations.

We adopt three fixed accretion radii in N-body units: $\xi_{\text{acc}} = 10^{-3}$, 10^{-4} , and 10^{-5} . We also run the model with $\xi_{\text{acc}} = 5 \times 10^{-5}$, which are used to extrapolate our simulation models to a realistic system (see section 4). The accretion radius we used here are larger than the tidal disruption radius, typically boosted by a factor of 10^{3-4} for the SMBH cases, because of our scaling requirements. We discuss this in Section 4.

Table 2 shows the simulation parameters and results. The first column shows each simulated model. The second, third, fourth, and fifth columns are the total number of N-body particles N in units of $K = 1024$, the normalized accretion radius ξ_{acc} , and the number of accreted particles N_{acc} entering inside the accretion radius, and the simulation run time t_{end} , respectively. The sixth and seventh columns describe the initial and final mass of the black hole normalized by M_c , respectively. Models 1-5 show the simulations for $\mu = 0.01$ case. Models 6-10 represent those for $\mu = 0.05$. Models 11-15 show the simulations for the growing black hole case with the initial value of $\mu = 0.01$. For the non-growing black hole case (Models 1-10), the simulations has been stopped when roughly one (or a few) percent of the stars are accreted, which is shorter than the half-mass relaxation time given by equation (4) of Zhong et al. (2014). This is because no black hole growth in spite of accretion can produce the artificial expansion of the cluster, leading to the unphysical effects. For the growing black hole case, t_{end} is limited for each model of Models 11-15 only by the computational resources, but is longer than the half-mass relaxation time except for Model 15. In the last five columns, we show the fractional number of the accreted particles on respective orbits in percent figures (%), where f_e , f_{me} , f_p , f_{mh} , and f_h are the fractional number of the eccentric, marginally eccentric, precisely parabolic, marginally hyperbolic, and hyperbolic TDEs, respectively (see Table 1 about the definition of each TDE).

3.2. Results

In this section, we describe the results of N-body simulations. The rate of accreted stars is defined by $\langle \dot{M}_{\text{acc}} \rangle = (M_c/t_{\text{end}})(N_{\text{acc}}/N)$, which is estimated to be 10^{-5} to 10^{-6} in simulation unit for all the models. All of our simulations do not reach the steady state for the rate. This is because the state of the loss cone, which controls the rate of accreted stars, changes with time. In the early phase, the loss cone is full as well as a density cusp forms around the central black hole, leading to an enhancement of the accretion rate. On the other hand, the empty loss cone leads to the reduction of the accretion rate in the late phase when a few half-mass relaxation time elapse (see also Figure 1 of Zhong et al. 2014).

Figures 2-4 show the dependence of the orbital eccentricity of the N-body particles, which accretes inside the accretion radius, on the penetration factor, β . Hereafter, we call it $e - \beta$ distribution of the accreted stars. In these figures, the black small circles represent $e - \beta$ distribution of the accreted N-body particles, whereas the black dashed line denotes $e = 1$. The red and blue solid lines show the critical eccentricities that are analytically expected from equations (5) and (6) with the fixed value of the mass ratio of the black hole to N-body particles, while the red and blue small circles show the two critical eccentricities of each N-body particle, which are numerically determined by substituting both β of each N-body particle and the mass ratio of the black hole to N-body particles into equations (5) and (6).

Figure 2 shows the $e - \beta$ distribution in Models 1-5. We confirm that the numerically calculated critical eccentricities are in good agreement with the analytically expected ones. In addition, almost all the accreted particles are distributed closely around $e = 1$ between two critical eccentricities. This means that eccentric and hyperbolic TDEs extremely rarely occur. For $\xi_{\text{acc}} = 10^{-4}$ cases (Models 2 and 4), the N-body particles are clearly distributed in the range of $e_{\text{crit},1} < e < e_{\text{crit},2}$. We note that a significant fraction of the accreted particles

will undertake the marginally eccentric and marginally hyperbolic TDEs. We also note from Figure 3 that the $e - \beta$ distributions of Models 6-10 qualitatively correspond to those of Models 1-5.

The $e - \beta$ distribution of the accreted stars in the growing black hole case is different from that of the fixed black hole mass case mainly in following two points. Figure 4 represents the $e - \beta$ distribution of the accreted stars in Models 11-15. The first point is that the numerically calculated critical eccentricities deviate from the analytically expected ones. In Models 11-15, the black hole mass increases with time by the accreted particles during the simulations. As seen in panel (b) of Figure 1, both of two critical eccentricities is closer to unity ($e=1$) with the growth of the black hole particle. The second point is that the number of more strongly bound N-body particles is larger than the fixed black hole case by comparison between panel (d) of Figure 2 and panel (d) of Figure 4. This is because the deeper gravitational potential of the black hole capture more the particles at a same distance from the black hole as that of the non-growth case. Moreover, some N-body particles clearly have the orbital eccentricity beyond the two critical eccentricities, as seen in panel (e). This is because the largest cross section makes it possible for the particles with the larger angular momentum to accrete onto the black hole than $\xi_{\text{acc}} = 10^{-4}$ and $\xi_{\text{acc}} = 10^{-5}$ cases.

Finally, let us see how the fraction of accreted particles is assigned to the types of eccentric, marginally eccentric, precisely parabolic, marginally hyperbolic, and hyperbolic TDEs. Because f_e , f_p , and f_h are very tiny as seen in the last five columns of Table 2, the eccentric, precisely parabolic, and hyperbolic TDEs are extremely rare events. Almost all of the accreted particles originate from N-body particles on marginally eccentric ($e_{\text{crit},1} \leq e < 1$) or marginally hyperbolic orbits ($1 < e \leq e_{\text{crit},2}$). We also find from the last five columns of Table 2 that the ratio of f_{me} to f_{mh} drastically changes. This can be

interpreted as follows: while all of the stars inside the influence radius of the central black hole, $r_h = GM_{\text{bh}}/\sigma^2$, where σ is the cluster’s velocity dispersion, are bounded to the black hole, the stars outside the influence radius are unbound to the black hole. According to the loss cone theory (Frank & Rees 1976; see also Merritt 2013 for a review), the stars are supplied to the black hole mainly from the critical radius, r_{crit} , where the opening angle of the loss cone angle $\theta_{\text{lc}} \approx \sqrt{r_t/r_{\text{crit}}}$ for $r \lesssim r_h$ is equal to the diffusion angle $\theta_{\text{D}} \propto \sqrt{\ln N/N}$. Because r_{crit} is proportional to $(N/\ln N)r_t$, it depends on each model. If r_{crit} is smaller than r_h , most of the accreted stars would be bound to cause marginally eccentric TDEs. Otherwise, they would be unbound to cause marginally hyperbolic TDEs. We will have more detailed discussion about this speculation in the forthcoming paper (Zhong et al. 2018).

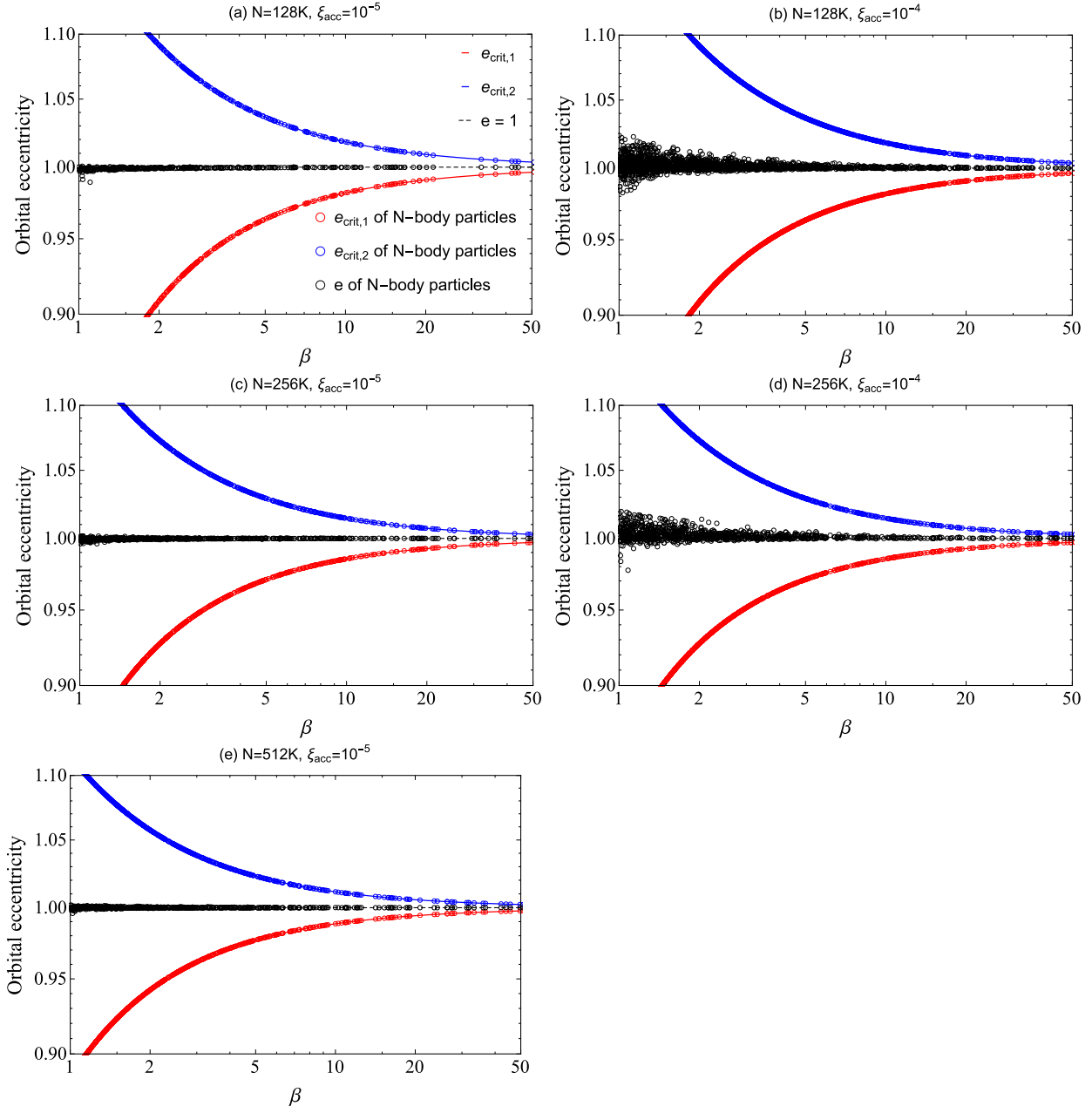


Fig. 2.— Dependence of critical and orbital eccentricities on the penetration factor β in the case of $\mu = 0.01$ (Models 1-5). While red and blue small circles represent the critical eccentricities of each accreted N-body particle for eccentric and hyperbolic TDEs, respectively. The black small circles show the orbital eccentricities of the accreted N-body particles. The black dashed line denotes $e = 1$, while the red and blue solid lines denote the corresponding analytically expected critical eccentricities.

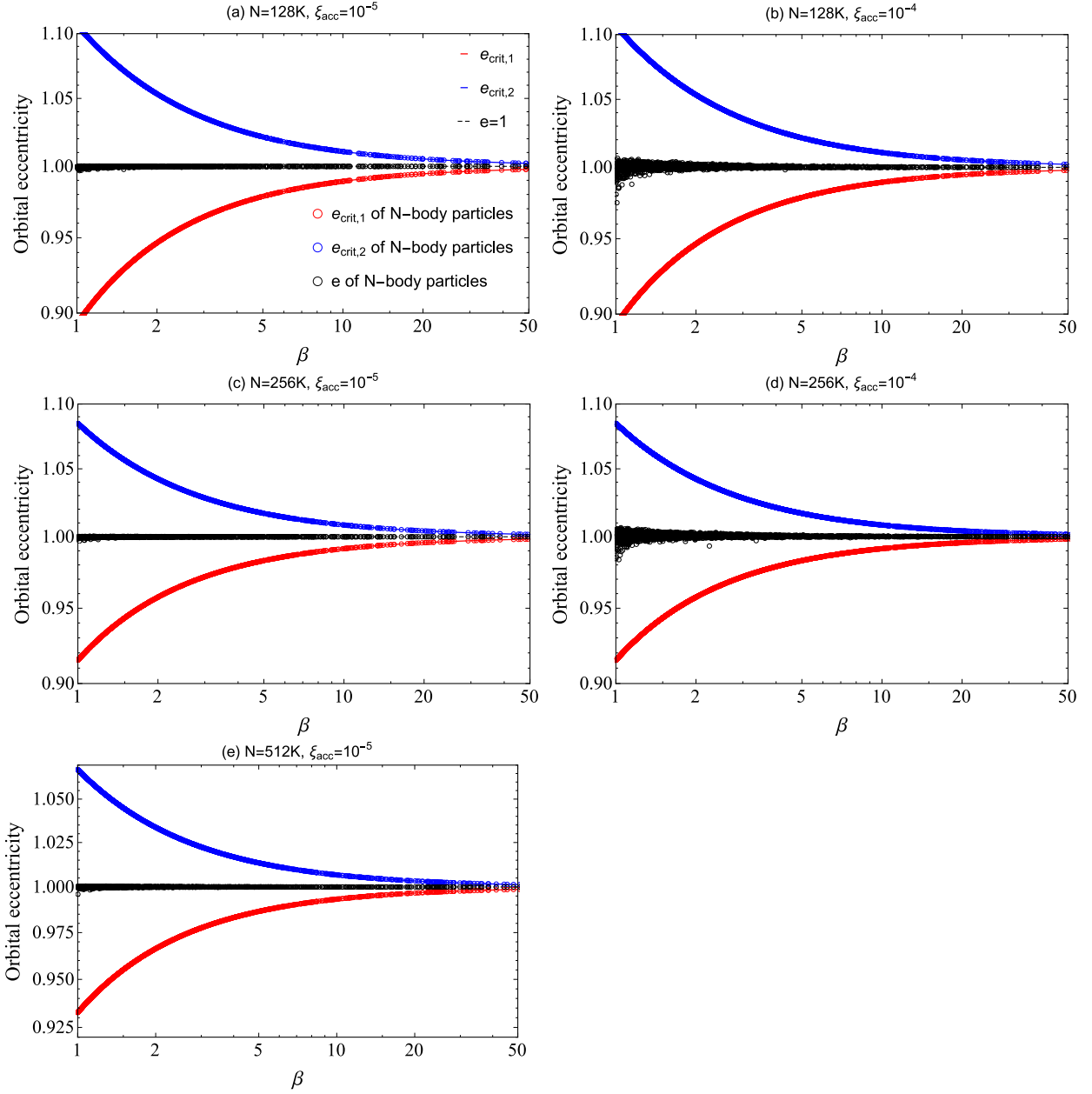


Fig. 3.— The same formats as Fig. 2 but for the case of $\mu = 0.05$ (Models 6-10).

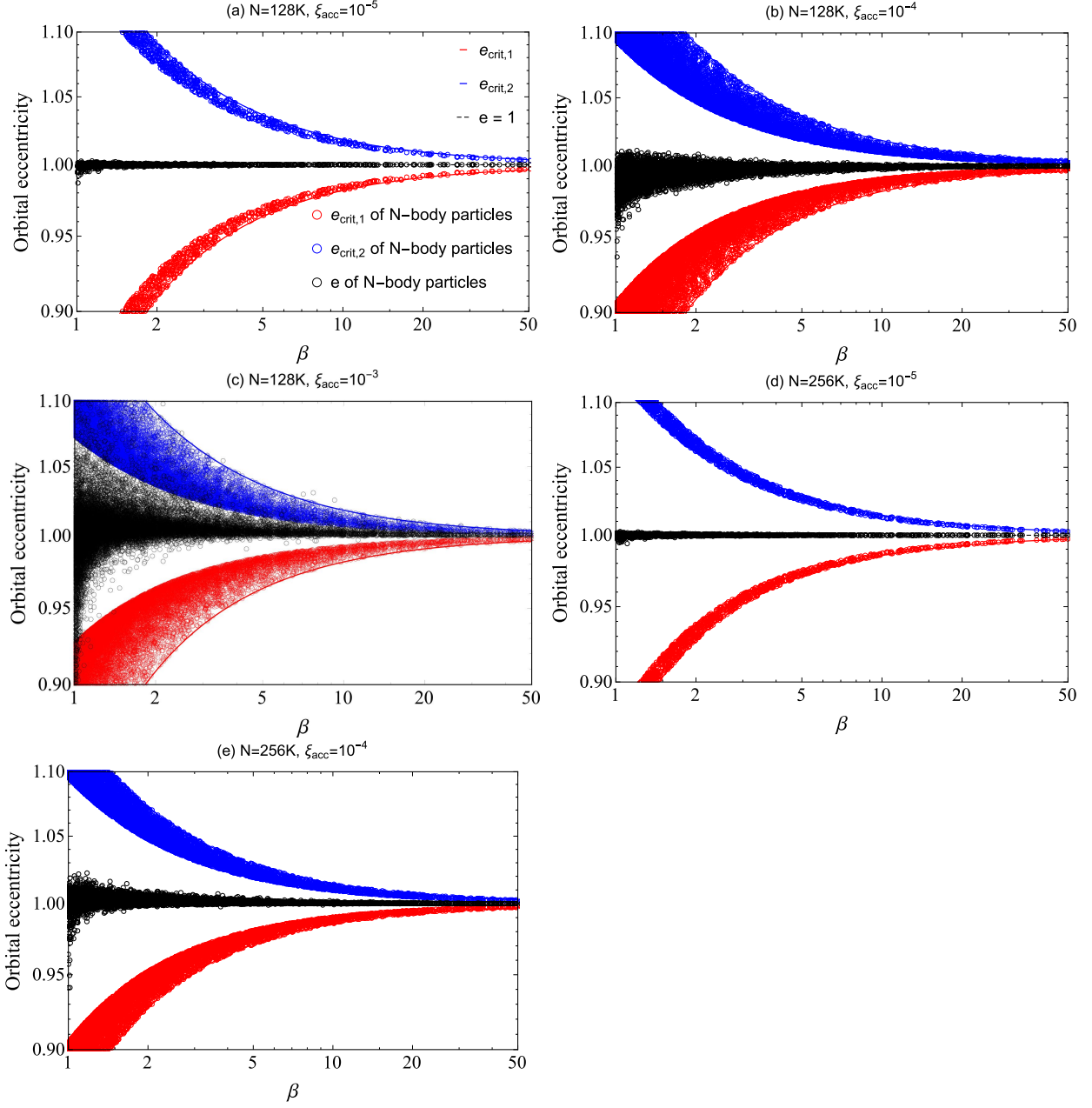


Fig. 4.— The same formats as Fig. 2 but for the case of the growing black hole initially from $\mu = 0.01$ (Models 11-15).

4. Discussion

In a realistic intermediate-mass to supermassive system, the tidal disruption radius should be smaller than $\xi_{\text{acc}} = 10^{-5}$, which is the smallest normalized accretion radius among our simulations, if the accretion radius is equal to tidal disruption radius. Therefore, we extrapolate from the simulation data the orbital eccentricities at the realistic value of ξ_{acc} and the higher particle resolution by the linear least-square fitting method; $y = cx + d$, where the fitted values are plugged in c and d , the mean value e_{mean} or standard deviation e_{std} of the orbital eccentricity are plugged in y , and the normalized accretion radius and the number of N-body particles are plugged in x , respectively. We define e_{mean} and e_{std} as follows: first, we divide the respective orbital eccentricities into some subsamples by a certain range of β , and then compute e_{mean} and e_{std} in each subsample. As one can see in the lower β region around $\beta \sim 1$, the different models show the significant variations, while in the higher β region they take almost the same values. Therefore, the data points within the range of $1 < \beta < 1.2$ are used to calculate e_{mean} and e_{std} .

Figure 5 shows the dependence of the mean value and the standard deviation of the simulated orbital eccentricity on the number of the N-body particles for the fixed value of $\xi_{\text{acc}} = 10^{-5}$ and $\mu = 0.01$ (Models 1, 3, and 5). The left and right panels are for e_{mean} and e_{std} , respectively. The eccentricity increases slightly with the higher mass resolution, whereas the standard deviation is smaller as the number of N-body particles increases. Figure 6 shows the dependence of the mean value and the standard deviation of the simulated orbital eccentricity on the normalized accretion radius for the fixed value of $N = 256\text{K}$ and $\mu = 0.01$ (Models 3 and 4). Note that we used $\xi_{\text{acc}} = 5 \times 10^{-5}$ case to get the argument more reliable. Both the mean value and standard deviation of the orbital eccentricity decrease with the normalized accretion radius. Overall, it is noted from the figures that the orbital eccentricity little deviates with the accretion radius and the number

of N-body particles from the mean value. This tendency can be adopted for the realistic extrapolated region, because the variation of the standard deviation is less than 0.1% for the given variables.

Next, in order to discuss how realistic the extrapolated values are, we introduce

$$\rho_{\text{bh}} \equiv M_{\text{bh}}/r_{\text{t}}^3 \quad (18)$$

as the black hole density estimated at the tidal disruption radius. With the three dimensionless parameters we previously defined; $\mu = M_{\text{bh}}/M_{\text{c}}$, $\xi_{\text{acc}} = r_{\text{acc}}/r_{\text{c}}$, and $\zeta = r_{\text{t}}/r_{\text{acc}}$, the black hole density can be rewritten as

$$\rho_{\text{bh}} = \mu \left(\frac{\zeta}{\xi_{\text{acc}}} \right)^3 \rho_{\text{c}}, \quad (19)$$

where $\rho_{\text{c}} \equiv M_{\text{c}}/r_{\text{c}}^3$ is defined as the mean stellar density of the cluster. Substituting equation (1) into (18), the black hole density is equivalent with the mean star density; $\rho_{*} \equiv m_{*}/r_{*}^3$. Therefore, the normalized mean star density can be given in two separated forms as

$$\frac{\rho_{*}}{\rho_{\text{c}}} = \begin{cases} \mu(\zeta/\xi_{\text{acc}})^3 = 1.0 \times 10^7 (0.01/\mu)^{-1} (1/\zeta)^{-3} (10^{-3}/\xi_{\text{acc}})^3 \\ (m_{*}/r_{*}^3)/\rho_{\text{c}} = 3.6 \times 10^{15} (\rho_{\text{c}}/10^8 M_{\odot} \text{pc}^{-3})^{-1} (m_{*}/M_{\odot})(r_{*}/R_{\odot})^{-3}. \end{cases} \quad (20)$$

The upper equation shows the normalized mean star density obtained from our simulation parameters, where we adopt $\zeta = 1$ which means that the accretion radius corresponds to the tidal disruption radius. In the lower equation, the normalized star density we estimate straightforwardly is constant for the accretion radius.

Figure 7 shows the dependence of the normalized mean star density on ξ_{acc} . The solid and dashed black lines are ρ_{*}/ρ_{c} , which is given by the upper part of equation (20), with $\mu = 0.01$ and $\mu = 0.05$, respectively. Assuming that $\rho_{\text{c}} = 10^8 M_{\odot} \text{pc}^{-3}$, the red and blue lines are ρ_{*}/ρ_{c} , which is given by the lower part of equation (20), with $(m_{*}, r_{*}) = (1 M_{\odot}, 1 R_{\odot})$ and $(m_{*}, r_{*}) = (10 M_{\odot}, 10 R_{\odot})$, respectively. The shaded area is the region where the cluster density would be realistic. Our simulation models ranges from $\xi_{\text{acc}} = 10^{-3}$ to 10^{-5} , whereas

the extrapolated range is less than $\xi_{\text{acc}} = 10^{-5}$. From the figure, we note that the range of $\xi_{\text{acc}} \lesssim 10^{-5}$ should be realistic, if the averaged density of the realistic star cluster composing of mainly early type stars is equal to $10^8 M_{\odot} \text{pc}^{-3}$. This is independent of whether the cluster has a SMBH or IMBH.

Let us discuss whether our extrapolation method is applicable to all the models we have done. To resolve the transition from full to empty loss cone, as predicted by the loss cone theory (Frank & Rees 1976; Merritt 2013), in direct N-body simulations, ξ_{acc} has to be consistent with the limited resolution by the finite particle number in the model. Too large ξ_{acc} means all loss cones are too large and never completely empty (always $\theta_{\text{lc}} > \theta_{\text{D}}$), and too small one means that we are always in the pinhole regime where $\theta_{\text{D}} > \theta_{\text{lc}}$. For given particle number N only a certain range of ξ_{acc} allows to resolve the correct full to empty loss cone transition at $\theta_{\text{lc}} = \theta_{\text{D}}$. Zhong et al. (2014) confirmed that our simulations are consistent with the loss cone theory, if the normalized accretion radius is less than $\xi_{\text{acc}} = 10^{-4}$. Therefore, we applied our extrapolation method only for the simulation models with the normalized accretion radius less than $\xi_{\text{acc}} = 10^{-4}$. Model 15 should be excluded from the extrapolation argument noted above, although it produces a tiny but interesting possibility to cause both eccentric and hyperbolic TDEs, as shown in Table 2.

As seen in panel (b) of Figure 1, the critical eccentricities are also closer to unity as the ratio of the central black hole to stellar mass is larger. This tendency can be seen in Figure 4: the simulated critical eccentricities is close to unity as the black hole mass increases with time, although it is limited to the very narrow range of the mass ratio. In the forthcoming paper, we will examine the broader range of the mass ratio.

It is interesting to see which marginally eccentric or hyperbolic TDEs more preferably occur. As discussed in Section 3.2, the source of the marginally eccentric TDEs is the stars falling to the black hole mainly from the critical radius inside the influence radius,

whereas the source of the marginally hyperbolic TDEs is the stars falling to the black hole mainly from the critical radius outside the influence radius. Therefore, the ratio of f_{me} and f_{mp} should be determined by the location of the critical radius relative to the influence radius. This suggests that $f_{\text{me}}/f_{\text{mp}}$ is close to unity if the stars have a recessed distribution symmetrically around the radius, where the influence radius is accordingly equal to the critical radius. Models 5 and 10 correspond to this case. Whether this argument is robust would be confirmed by performing higher particle resolution N-body experiments with smaller accretion radius.

The deviation between some observed optical-UV TDEs light curves and the $t^{-5/3}$ decline rate is currently topics of debate (e.g. Gezari et al. 2012). Also, the soft X-ray TDE candidate represents the slightly different power law decay from $t^{-5/3}$ (Maksym et al. 2013), although it looks corresponding to the $t^{-5/3}$ curve overall. Assuming that the observed luminosity is simply proportional to t^{-n} , we find

$$n = \frac{2\alpha + 5}{3} \quad (21)$$

from our conjecture of the mass fallback rate given by equation (16). We note from Table 1 that the possible range of n is $1 < n \leq 5/3$ for the marginally eccentric and marginally hyperbolic TDEs. Gezari et al. (2012) discussed that the value of n fitted to the decay of PS1-10jh was estimated to be $n = 5/9$, $35/36$, and $12/15$ for the respective flaring phases. Because these indices are less than unity, our conjecture is not appropriate for PS1-10jh case. The other optical-UV TDE candidate, J0225-0432, represented that a best fit for the value of n to the UV data gives $n \approx 1.1$ (Gezari et al. 2008). In this case, we cannot reject the possibility that J0225-0432 is a candidate for the marginally eccentric or marginally hyperbolic TDEs. This is also consistent with that the light curve of J0225-0432 should be shallower than the $t^{-5/3}$ profile by the internal structure of the star, as argued by Lodato et al. (2009). If the star is partially disrupted, the range of n can be from 2.2 to 4 because

of the centrally condensed mass distribution, leading to the steeper mass fallback rate (Guillochon & Ramirez-Ruiz 2013). This case is also beyond the scope of our conjecture. It suggests that the differential mass distribution should follow no simple power law of the specific energy. We need to rebuild the conjecture by taking account of the detailed internal structure of the star or the stellar debris.

Although these arguments seem independent of the semi-major axis and orbital eccentricity of the star approaching to the black hole, the difference between precisely parabolic and marginally eccentric/hyperbolic TDEs is shown in the magnitude of the mass fallback rate for a given value of α . In addition, the value of α can depend on the semi-major axis and the orbital eccentricity as Hayasaki et al. (2013) implied. There is little known whether and how it can depend on them, and is no direct estimation of α . Therefore, it is desired to examine the dependence of α on the given semi-major axis and orbital eccentricity in detail by the hydrodynamic simulations.

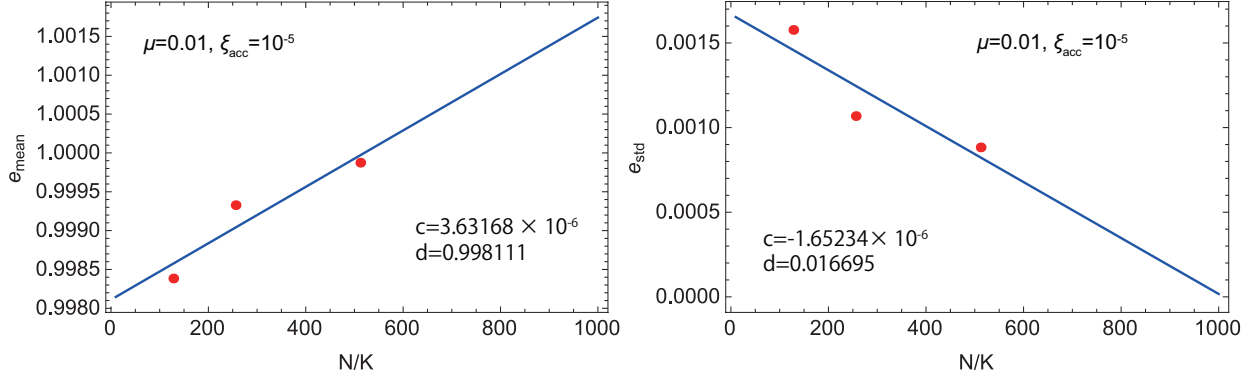


Fig. 5.— Dependence of the mean value and standard deviation of the orbital eccentricity on the number of the N-body particles for $\mu = 0.01$ and $\xi_{\text{acc}} = 10^{-5}$. The red points shows them by numerical simulations, while the blue line shows the linear fitting by the least-square method; $y = cx + d$, where $y = e_{\text{mean}}$ or e_{std} and $x = N/K$, respectively.

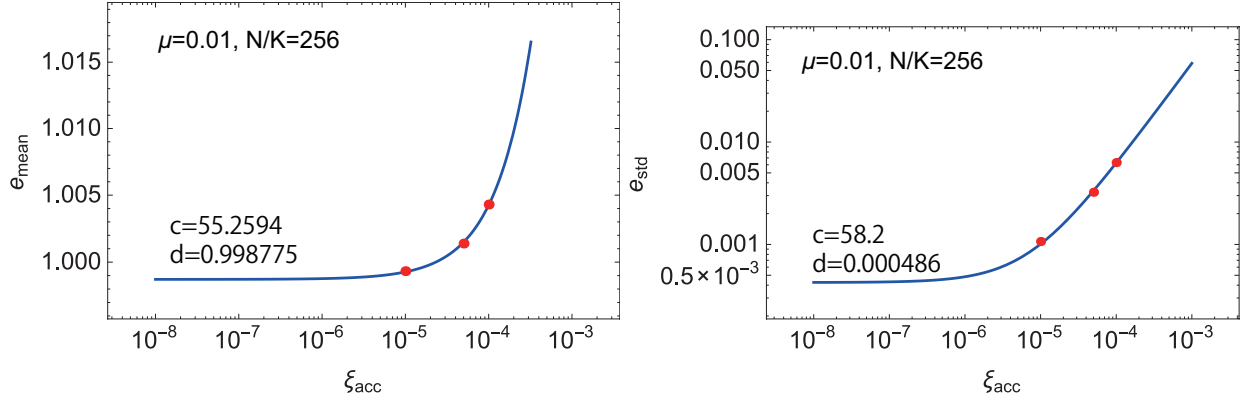


Fig. 6.— Dependence of the mean value and standard deviation of the orbital eccentricity on the normalized accretion radius for $\mu = 0.01$ and $N/K = 256$. The red points shows them by numerical simulations, while the blue line shows the linear fitting by the least-square method; $y = cx + d$, where $y = e_{\text{mean}}$ or e_{std} and $x = \xi_{\text{acc}}$, respectively.

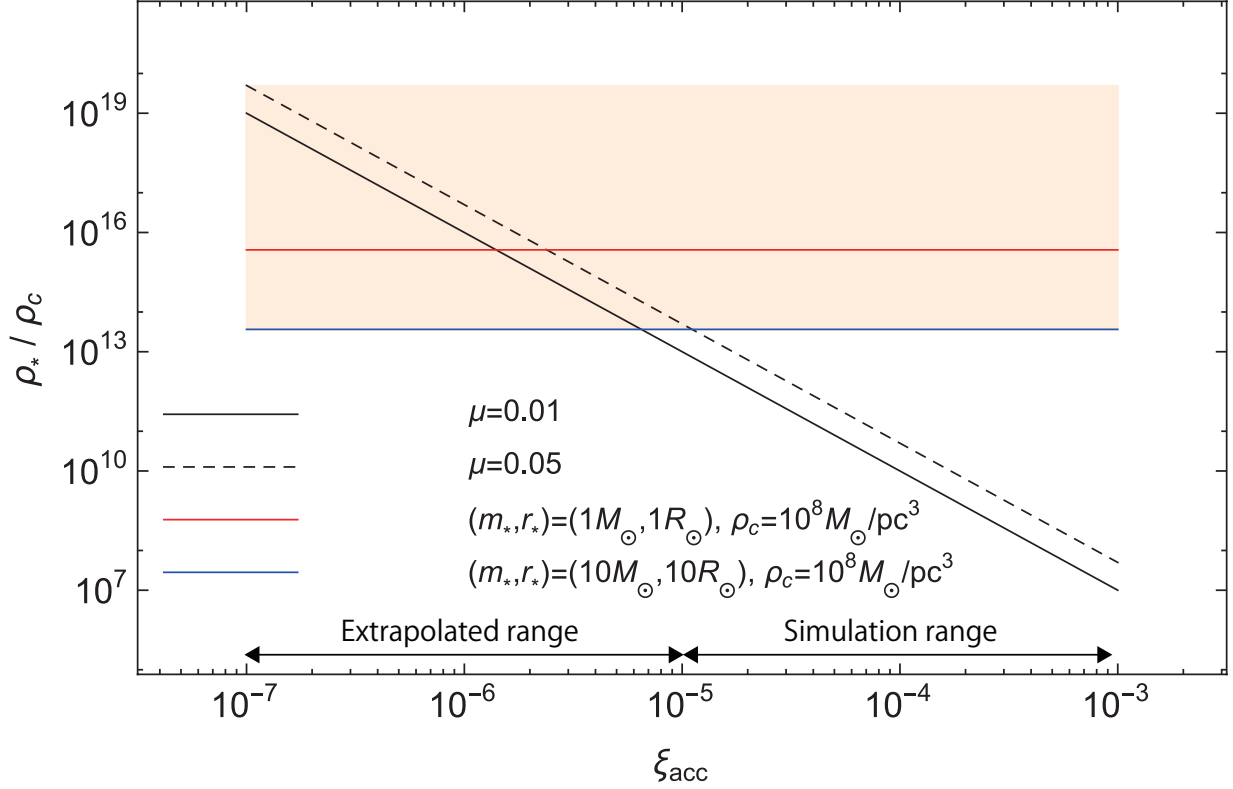


Fig. 7.— Dependence of the mean density of a star normalized by stellar density of a cluster on the accretion radius. The solid and dashed black lines are the normalized mean star density in the case of $\mu = 0.01$ and $\mu = 0.05$, respectively. The red and blue lines are those with $(m_*, r_*) = (1 M_\odot, 1 R_\odot)$ and $(m_*, r_*) = (10 M_\odot, 10 R_\odot)$, respectively, when $\rho_c = 10^8 M_\odot \text{pc}^{-3}$. The shaded area is the region where the stellar density of the cluster would be realistic. Our simulation models range from $\xi_{\text{acc}} = 10^{-3}$ to 10^{-5} , whereas the extrapolated range is smaller than $\xi_{\text{acc}} = 10^{-5}$.

5. Conclusions

We have investigated the distribution of the orbital eccentricity of stars approaching the intermediate to supermassive black holes by N-body experiments. Since our N-body models do not reach a realistic resolution in particle number N for galactic nuclei and consequently also cannot resolve the realistic value of the tidal disruption radius, we have used the method of scaling to extrapolate our results to the situation of a real galactic nucleus or nuclear stellar cluster. We have also found the condition to categorize the TDEs into the three types: eccentric, parabolic, and hyperbolic TDEs, from the viewpoints of the orbital eccentricity, e and the semi-major axis of the originally approaching star, a . Based on the condition, we have analytically derived the mass fallback rates of respective TDEs. Our main conclusions are summarized as follows:

1. Parabolic TDEs are moreover divided into three subclasses: TDEs from stars on precisely parabolic orbits ($e = 1$), marginally eccentric TDEs ($e_{\text{crit},1} \leq e < 1$), and marginally hyperbolic TDEs ($1 < e \leq e_{\text{crit},2}$). While the mass fallback rate of marginally eccentric TDEs can be flatter and slightly higher than the standard fallback rate proportional to $t^{-5/3}$, it can be flatter and lower for marginally hyperbolic TDEs. The detail is summarized in Table 1.
2. We find that there are two critical values of the orbital eccentricity: $e_{\text{crit},1} = 1 - 2q^{-1/3}/\beta$ below which eccentric TDEs occur, and $e_{\text{crit},2} = 1 + 2q^{-1/3}/\beta$ above which hyperbolic TDEs occur, where q is the ratio of black hole to stellar mass and β is the penetration factor. As the mass ratio is more extreme and the pericenter distance is closer to the Schwarzschild radius, these critical eccentricities are closer to 1. We confirm from our simulations that these critical eccentricities vary as the black hole grows.
3. Alternatively, there is a critical value of semi-major axis: $a_c = 50(q/10^6)^{1/3}r_t$, where

r_t is the tidal disruption radius. If $a \leq a_c$, then the eccentric and hyperbolic TDEs would occur. However, we confirm by N-body experiments that eccentric, precisely parabolic, and hyperbolic TDEs extremely rarely occur in a spherical stellar system with a single intermediate-mass to supermassive black hole. Instead, a substantial fraction of the stars causes marginally eccentric or marginally hyperbolic TDEs.

Acknowledgments

The authors thank the anonymous referee for fruitful comments and suggestions. The authors also thank Nicholas C. Stone for his helpful comments and suggestions. This research has been supported by the Korea Astronomy and Space Science Institute (KASI) under the R&D program supervised by the Ministry of Science, ICT and Future Planning and by Basic Science Research Program through the National Research Foundation of Korea (NRF) funded by the Ministry of Education (NRF-2017R1D1A1B03028580 K.H.). Data reductions were performed by using a high performance computing cluster at the KASI. Authors acknowledge support by the Chinese Academy of Sciences (CAS) through the Silk Road Project at NAOC, through the CAS Visiting Professorship for Senior International Scientists, Grant Number 2009S1-5 (R.S.), and through the 'Qianren' special foreign experts programme of China. S.Z., S.L., and R.S. have been partially supported by National Natural Science Foundation of China (NSFC 11603067 S.Z., 11303039 S.L., and 11673032 R.S.). P.B. acknowledges the special support by the NASU under the Main Astronomical Observatory GRID/GPU computing cluster project. The special GPU accelerated supercomputer laohu at the Center of Information and Computing at National Astronomical Observatories, CAS, funded by Ministry of Finance of People's Republic of China under the grant ZDYZ2008-2 has been used for computer simulations. S.L. P.B., and R.S. acknowledge also the Strategic Priority Research Program (PilotB) "Multi-waveband

Gravitational Wave Universe” of the CAS (No. XDB23040100).

REFERENCES

- Aarseth, S. J., Henon, M., Wielen, R., 1974, *A&A*, 37, 183
- Alexander, K. D., Berger, E., Guillochon, J., Zauderer, B. A., & Williams, P. K. G. 2016, *ApJ*, 819, L25
- Arcavi I. et al., 2014, *ApJ*, 793, 38
- Auchettl, K., Guillochon, J., & Ramirez-Ruiz, E. 2017, *ApJ*, 838, 149
- Bahcall, J. N., Wolf, R. A. 1976, *ApJ*, 209, 214
- Baumgardt, H., Makino, J., & Ebisuzaki, T. 2004, *ApJ*, 613, 1133
- Berczik, P., Nitadori, K., Zhong, S., Spurzem, R., Hamada, T., Wang, X., Berentzen, I., Veles, A., and Ge, W. 2011, in International conference on High Performance Computing, Kyiv, Ukraine, October 8-10, 2011., p. 8-18
- Berczik, P., Spurzem, R., Wang, L., Zhong, S., Huang, S. 2013, Third International Conference “High Performance Computing”, HPC-UA 2013, p. 52-59, 52
- Berczik, P., Spurzem, R., Zhong, S., Wang, L., Nitadori, K., Hamada, T., Veles, A. 2013, in Lecture Notes in Computer Science, Vol. 7905, Procs. of 28th Intl. Supercomputing Conf. ISC 2013, Leipzig, Germany, June 16-20, 2013., ed. J. M. Kunkel, T. Ludwig, and H. E. Meuer (Springer Vlg.), 13-25
- Bonnerot, C., Rossi, E. M., & Lodato, G. 2017, *MNRAS*, 464, 2816
- Brockamp, M., Baumgardt, H., Kroupa, P. 2011, *MNRAS*, 418, 1308
- Brown, G. C., Levan, A. J., Stanway, E. R., et al. 2015, *MNRAS*, 452, 4297
- Burrows D. N. et al., 2011, *Nature* 476, 421

- Chornock, R., Berger, E., Gezari, S., et al. 2014, *ApJ*, 780, 44
- Coughlin, E. R., & Nixon, C. 2015, *ApJ*, 808, L11
- Donley J. L., Brandt W. N., Eracleous M., Boller T., 2002, *AJ*, 124, 1308
- Evans C.R., Kochanek C.S., 1989, *ApJ*, 346, L13
- Frank, J., Rees, M. J. 1976, *MNRAS*, 176, 633
- Farrar, G. R., & Piran, T. 2014, arXiv:1411.0704
- Gezari, S., Martin, D. C., Milliard, B., et al. 2006, *ApJ*, 653, L25
- Gezari, S., Basa, S., Martin, D. C., et al. 2008, *ApJ*, 676, 944-969
- Gezari S. et al., 2012, *Nature*, 485, 217
- Guillochon, J., & Ramirez-Ruiz, E. 2013, *ApJ*, 767, 25
- Harfst, S., Gualandris, A., Merritt, D., et al. 2007, *New A*, 12, 357
- Hayasaki, K., Stone, N., Loeb, A. 2013, *MNRAS*, 434, 909
- Hayasaki, K., Stone, N., Loeb, A. 2016, *MNRAS*, 461, 3760
- Heggie, D. C., Mathieu, R. D., 1986, in *Lecture Notes in Physics*, Berlin Springer Verlag,
Vol. 267, *The Use of Supercomputers in Stellar Dynamics*, ed. P. Hut & S. L. W.
McMillan, 233
- Hénon, M. 1971, *Ap&SS*, 13, 284
- Holoien, T. W.-S., Prieto, J. L., Bersier, D., et al. 2014, *MNRAS*, 445, 3263
- Hung, T., Gezari, S., Blagorodnova, N., et al. 2017, *ApJ*, 842, 29

- Jiang, Y.-F., Guillochon, J., & Loeb, A. 2016, *ApJ*, 830, 125
- Just, A., Yurin, D., Makukov, M., et al. 2012, *ApJ*, 758, 51
- Kennedy, G. F., Meiron, Y., Shukirgaliyev, B., et al. 2016, *MNRAS*, 460, 240
- Khan, F. M., Berentzen, I., Berczik, P., Just, A., Mayer, L., Nitadori, K., Callegari, S. 2012, *ApJ*, 756, 30
- Khan, F. M., Fiacconi, D., Mayer, L., Berczik, P., Just, A. 2016, *ApJ*, 828, 73
- Komossa S., Bade N., 1999, *A&A*, 343, 775
- Komossa, S. 2015, *Journal of High Energy Astrophysics*, 7, 148
- Li, S., Liu, F. K., Berczik, P., & Spurzem, R. 2017, *ApJ*, 834, 195
- Lodato, G., King, A.R., Pringle, J.E. 2009, 392, 332
- Lodato G., Rossi E. M., 2011, *MNRAS*, 410, 359
- Magorrian, J., Tremaine, S., Richstone, D., et al., 1998, *AJ* 115, 2285
- Magorrian, J., Tremaine, S., 1999, *MNRAS*, 309, 447
- Maksym, W. P., Ulmer, M. P., Eracleous, M. C., Guennou, L., & Ho, L. C. 2013, *MNRAS*, 435, 1904
- McConnell, N. J., Ma, C.-P., 2013, *ApJ*, 764, 184
- Merritt, D. 2013, *Classical and Quantum Gravity*, 30, 244005
- Phinney, E. S. 1989, in *IAU Symp. 136, The Center of the Galaxy*, ed. M. Morris (Dordrecht: Kluwer Academic Publishers), 543
- Piran, T., Svirski, G., Krolik, J., Cheng, R. M., & Shiokawa, H. 2015, *ApJ*, 806, 164

- Rees, M. J., 1998, *Nature* 333, 523
- Saxton, R. D., Read, A. M., Esquej, P., et al. 2012, *A&A*, 541, A106
- Spurzem, R., Berczik, P., Zhong, S., Nitadori, K., Hamada, T., Berentzen, I., Veles, A. 2012, in *Astronomical Society of the Pacific Conference Series*, Vol. 453, *Advances in Computational Astrophysics: Methods, Tools, and Outcome*, ed. R. Capuzzo-Dolcetta, M. Limongi, and A. Tornambé, 223
- Stone, N., Metzger, B. D. 2016, *MNRAS*, 455, 859
- Strubbe, L. E., & Quataert, E. 2009, *MNRAS*, 400, 2070
- van Velzen, S., Farrar, G. R., 2014, *ApJ*, 792, 53
- van Velzen, S., Anderson, G. E., Stone, N. C., et al. 2016, *Science*, 351, 62
- Vinkó, J., Yuan, F., Quimby, R. M., et al. 2015, *ApJ*, 798, 12
- Wang, J., Merritt, D., 2004, *ApJ*, 600, 149
- Zauderer B. A., et al., 2011, *Nature* 476, 425
- Zhong, S., Berczik, P., Spurzem, R. 2014, *ApJ*, 792, 137
- Zhong, S., et al. 2018, in prep.